Magnetic field amplification and flat spectrum radio quasars

Xuhui Chen,[1,2]★ Ritaban Chatterjee,[3] Haocheng Zhang,[4,5] Martin Pohl,[1,2] Giovanni Fossati,[6] Markus Böttcher,[7,4] Charles D. Bailyn,[8] Erin W. Bonning,[9] Michelle Buxton,[8] Paolo Coppi,[8] Jedidah Isler,[8] Laura Maraschi[10] and Meg Urry[11]

[1]*Institute of Physics and Astronomy, University of Potsdam, D-14476 Potsdam-Golm, Germany*

[2]*DESY, Platanenallee 6, D-15738 Zeuthen, Germany*

[3]*Department of Physics, Presidency University, 86/1, College street, Kolkata-700073, India*

[4]*Astrophysical Institute, Department of Physics and Astronomy, Ohio University, Athens, OH 45701, USA*

[5]*Theoretical Division, Los Alamos National Laboratory, Los Alamos, NM 87545, USA*

[6]*Department of Physics and Astronomy, Rice University, Houston, TX 77005, USA*

[7]*Centre for Space Research, North-West University, Potchefstroom 2520, South Africa*

[8]*Department of Astronomy, Yale University, PO Box 208101, New Haven, CT 06520-8101, USA*

[9]*Department of Physics, Emory University, Atlanta, GA 30322, USA*

[10]*INAFOsservatorio Astronomico di Brera, V. Brera 28, I-20100 Milano, Italy*

[11]*Department of Physics and Yale Center for Astronomy and Astrophysics, Yale University, PO Box 208121, New Haven, CT 06520-8121, USA*

ABSTRACT

We perform time-dependent, spatially resolved simulations of blazar emission to evaluate several flaring scenarios related to magnetic-field amplification and enhanced particle acceleration. The code explicitly accounts for light-travel-time effects and is applied to flares observed in the flat spectrum radio quasar (FSRQ) PKS 0208−512, which show optical/γ-ray correlation at some times, but orphan optical flares at other times. Changes in both the magnetic field and the particle acceleration efficiency are explored as causes of flares. Generally, external Compton (EC) emission appears to describe the available data better than a synchrotron self-Compton (SSC) scenario, and in particular orphan optical flares are difficult to produce in the SSC framework. X-ray soft-excesses, γ-ray spectral hardening, and the detections at very high energies of certain FSRQs during flares find natural explanations in the EC scenario with particle acceleration change. Likewise, optical flares with/without γ-ray counterparts can be explained by different allocations of energy between the magnetization and particle acceleration, which may be related to the orientation of the magnetic field relative to the jet flow. We also calculate the degree of linear polarization and polarization angle as a function of time for a jet with helical magnetic field. Tightening of the magnetic helix immediately downstream of the jet perturbations, where flares occur, can be sufficient to explain the increases in the degree of polarization and a rotation by $\geq 180°$ of the observed polarization angle, if light-travel-time effects are properly considered.

Key words: radiation mechanisms: non-thermal – galaxies: active – galaxies: jets – quasars: individual: PKS 0208-512.

1 INTRODUCTION

As an extreme class of active galactic nuclei (AGNs), blazars are known to emit electromagnetic waves in almost all frequencies that are currently being observed, extending from radio to γ-ray. They are also famous for being highly variable in an unpredictable manner. An interesting question is whether blazar variations at different wavelengths are correlated, and if so, how. For example, whether

there are any time lags, what the amplitude relations are. The answers to these questions can, e.g. identify the location and mechanism of emission. For one type of blazars, namely, flat spectrum radio quasars (FSRQs), the correlation between optical emission and GeV γ-rays is particularly interesting. These two energy bands represent the energies either at or beyond the peaks of the two components of their spectral energy distributions (SEDs; Sambruna, Maraschi & Urry [1996]). The photons in these energies are probably emitted by the most energetic particles, and hence exhibit most violent variations. Identification of these correlations became possible following the launch of *Fermi* and the implementation of its

★ E-mail: chenxuhui.phys@gmail.com

supporting optical monitoring programmes, such as the Yale/SMARTS programme.

In most cases, the correlation between these two bands are established (Bonning et al. 2012; Chatterjee et al. 2012). However, Chatterjee et al. (2013a) identified at least one case of such correlation breaking down (see also fig. 2 of H.E.S.S. Collaboration 2013). In contrast to the 'orphan' γ-ray flares occasionally found in BL Lac objects (Krawczynski et al. 2004), these FSRQs show strong optical flares without γ-ray counterparts. The authors of Chatterjee et al. (2013a) identified three major optical flares from PKS 0208−512 over a period of three years. γ-ray activity in flares 1 and 3 is highly correlated with that at the optical band. But in flare 2, the γ-ray flux remains at a low level. The question arises why the same source exhibits correlated optical/γ-ray flares sometimes, but orphan optical flares at other times.

Since the optical emission is generally accepted to be produced by synchrotron emission (Bregman et al. 1981; Urry & Mushotzky 1982; Impey & Neugebauer 1988; Marscher 1998), it is sensible to postulate that if the flare is caused by a change of the magnetic field, it may not have a direct effect on the γ-ray emission, except the indirect effect through particle cooling and acceleration. It is known that magnetic field can be amplified by astrophysical shocks beyond simple shock compression through a turbulent dynamo effect. This has been proved both numerically (Guo et al. 2012) and analytically (Fraschetti 2013), and has been applied to explain observations of supernova remnants (SNRs; Parizot et al. 2006) and γ-ray bursts (GRBs; Mizuno et al. 2011). If this kind of amplification is also at work in relativistic jets which presumably harbour blazar flares, it can be expected to explain the orphan optical flares.

Chatterjee, Nalewajko & Myers (2013b) studied these anomalous flares of PKS 0208−512 with a time-independent model. However, since blazar flares are naturally time-dependent phenomena, it is important to account for the timing information with time-dependent modelling. We will briefly describe the data reduction and analysis in Section 2. The comparison between time-dependent modelling and the observation are presented in Section 4, followed by discussion in Section 5.

2 MULTIWAVELENGTH DATA OF PKS 0208−512

PKS 0208−512 is a high-power blazar with redshift of 1.003. It has been classified as a BL Lac object based on its line properties (Healey et al. 2008). However, Ghisellini et al. (2011) noted that the broad-line emission from PKS 0208−512 is in fact strong ($L_{\rm Mg\,II} \sim 10^{44}$ erg s^{-1}), on top of the fact that the SED of this source resembles those of FSRQs. So it is suggested that this source should be reclassified as an FSRQ.

We obtained spectra of PKS 0208−512 at the MeV–GeV energy range by analysing data from *Fermi*/large area telescope (LAT). For this purpose, we used the standard *Fermi*/LAT Science Tools software package (version v9r27p1). We analysed a region of interest of 15° in radius, centred at the position of PKS 0208−512, using the maximum likelihood algorithm implemented in `gtlike`. We included all sources within 15° of PKS 0208−512, extracted from the *Fermi* 2 yr catalogue (2FGL), with their normalizations kept free and spectral indices fixed to their catalogue values. We use the data selection P7SOURCE_V6 and its response functions, the diffuse background model `gal_2yearp7v6_v0.fits`, and the isotropic background model `iso_p7v6source.txt`. To calculate the spectra, we divide the spectral range 0.1–24.3 GeV into two spectral bins and model PKS 0208−512 with a simple power law

at each spectral bin with the spectral index and normalization kept free. We obtained the γ-ray spectra at various 10 d intervals during flares 1 and 3 (as defined in Chatterjee et al. 2013a) in order to probe the spectral changes during the rise and decay of those outbursts. Smaller time intervals cannot always give two spectral points with enough statistical significance, while larger time intervals cannot resolve the profile of the flares.

Light curves in the *B*, *V*, *R*, *J*, and *K* band are from the Yale/SMARTS optical–near-infrared blazar monitoring program[1] (Bonning et al. 2012; Chatterjee et al. 2012), which uses the ANDICAM (A Novel Dual Imaging CAMera) instrument on the SMARTS 1.3 m telescope located at Cerro Tololo Inter-American Observatory (CTIO), Chile. Details of observations and data reduction procedures are described in Bonning et al. (2012). We calculate the Optical Infrared (OIR) SEDs and light curves by averaging the flux over 10 d intervals.

We obtained the X-ray data from the *Swift*/X-ray Telescope (XRT) monitoring program of *Fermi*/LAT sources of interest[2] (Stroh & Falcone 2013). We use the *Swift*/XRT data products generator[3] (Evans et al. 2009), and fitted the data with the X-ray spectral fitting package XSPEC. During the time interval of interest (MJD 551 90– 552 00, high state of flare 2), *Swift*-XRT only observed the source for one 1351 s period on MJD 551 95.

The high- and low-state SEDs from flares 1 and 2 are shown with the simulation results in Figs 4–7. In Fig. 1, we show the light curves of the three flares identified by Chatterjee et al. (2013a). Note that flare 3 can also be viewed as an ensemble of two flares peaking at MJD 557 35 and 558 15. The light curves of flares 1 and 3 in optical and γ-rays show striking similarity with no apparent delay between the peaks at different energies. Flare 2 is not significantly detected in γ-rays in 10 d bins. We show its optical light curves together with the simulation results.

3 THE MODEL

We use the time-dependent multizone blazar model built by Chen et al. (2011, 2012) to study the multiwavelength data set of PKS 0208−512. This model employs an axisymmetric cylindrical geometry (see Fig. 2), divided into many zones in radial and longitudinal directions to account for inhomogeneity. This inhomogeneous blob, whose emission is assumed to dominate over the continous jet stream because of higher density and/or stronger magnetic field, travels relativistically in the AGN frame and encounters a stationary perturbation that, for simplicity, is treated as a flat feature. In the blob frame, it is the perturbation that travels through the blob and causes a change in the plasma condition, hence initiating the flare. The model is based on our 2-D Monte Carlo/Fokker–Planck (MCFP) code. The Monte Carlo technique is used for the radiative transfer, so that all light-travel-time effects (LTTEs) are taken into account.

The temporal evolution of the electron (and positron) population in each simulation zone is obtained by solving the Fokker–Planck equation for the differential number density of electrons, $N(\gamma, t)$:

$$\frac{\partial N(\gamma, t)}{\partial t} = -\frac{\partial}{\partial \gamma}[N(\gamma, t)\dot{\gamma}(\gamma, t)] + \frac{\partial}{\partial \gamma}\left[D(\gamma, t)\frac{\partial N(\gamma, t)}{\partial \gamma}\right]$$

$$+ Q(\gamma, t) - \frac{N(\gamma, t)}{t_{\rm esc}}. \tag{1}$$

---

[1] http://www.astro.yale.edu/smarts/fermi/

[2] http://www.swift.psu.edu/monitoring/

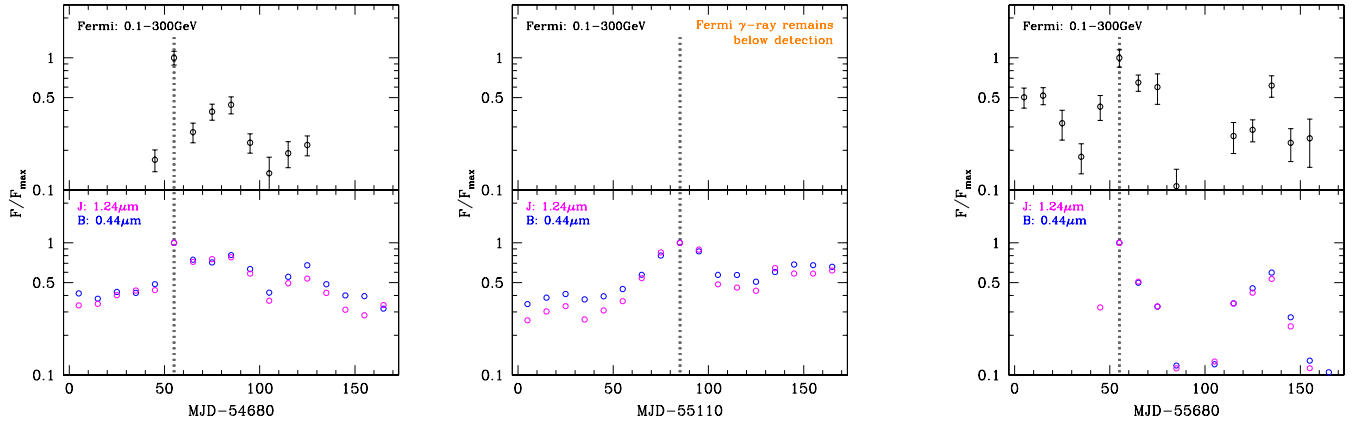[3] http://www.swift.ac.uk/user_objects/docs.php

Figure 1. *Fermi* (upper panels) and SMARTS (lower panels) optical/near-infrared light curves in 10d bins. From left to right, the figures cover flares 1, 2, and 3 identified by Chatterjee et al. (2013a), starting from Modified Julian Date (MJD) 546 80, 551 10, and 556 80. The flare peaks are marked with dotted lines.
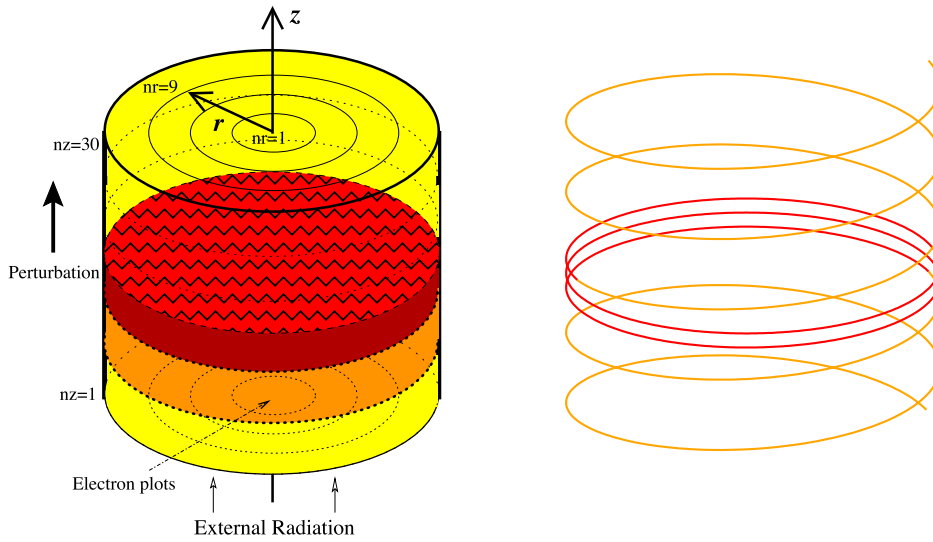

Figure 2. Left: sketch of the model geometry and its comoving 2-D grid with azimuthal symmetry. The hatched layer represents a perturbation that is stationary in the black hole frame and relativistically moving upward in the blob rest frame. The yellow zones represent quiescent regions in which the particles have reached equilibrium between acceleration and losses. We plot in red the zones in which the magnetic field or the acceleration efficiency have changed to induce a flare. The orange zones represent the regions in which the gain and loss rates are back to their baseline levels, but particle spectra have not fully recovered. Right: a sketch of the helical magnetic field used in Section 4.3. The red portion of the field line stands for the perturbed region, where an enhancement of the azimuthal component of the field leads to the tightening of the helix, and hence a change in the field direction.

On the right-hand side of equation (1), the first term describes continuous cooling and acceleration of the particles with rate $\dot{\gamma}$,

$$\dot{\gamma}(\gamma, t) = \dot{\gamma}_{\text{cool}}(\gamma, t) + \dot{\gamma}_D(\gamma, t), \qquad (2)$$

which includes stochastic particle acceleration with rate

$$\dot{\gamma}_D(\gamma, t) = \frac{2}{\gamma} D(\gamma, t) = \frac{\gamma}{t_{\text{acc}}}, \qquad (3)$$

for which the acceleration time-scale is defined by t_{acc}.

The second term describes the diffusion of the particle in momentum space with diffusion coefficient

$$D(\gamma, t) = \frac{\gamma^2}{2 t_{\text{acc}}}. \qquad (4)$$

The acceleration process is similar to that described by Katarzyński et al. (2006). It is a result of particle diffusion in momentum space, which mainly represents the second-order *Fermi* process. The

acceleration time-scale is assumed to be independent of particle energy here. One can also reasonably assume that the acceleration time-scale changes with particle energy, e.g. it increases linearly with energy. The resulted particle spectrum will deviate from a simple power law. A detailed study of an energy-dependent acceleration will be the subject of a separate publication.

The third term of equation (1), $Q(\gamma, t)$, describes particle injection; the fourth term accounts for particle escape through an adjustable parameter t_{esc} that is not changed throughout the simulation.

The quiescent state of the jet is established through quasi-monoenergetic injection at Lorentz factors γ_{inj} which is technically realized with a narrow Gaussian. Such injection spectra may arise from sweep-up of ambient material by a fast plasma cloud (Pohl & Schlickeiser 2000), in quasi-perpendicular relativistic shocks, or through the pile-up effect caused by the balance between *Fermi* acceleration and radiative cooling (Schlickeiser 1984). But here it

Table 1. The parameters used for the quiescent state. The observation angle is always $1/\Gamma$ so that the Doppler factor δ is equal to the bulk Lorentz factor Γ. The volume radius $R = 3Z/4$ in all cases. The time-scale for acceleration and escape have the ratio $t_{acc}/t_{esc} = 6.5$, except during the flare caused by excess acceleration.

	SSC	EC
B(G)	3.8×10^{-4}	2
δ	40	40
γ_{inj}	2.4×10^3	20
Z(cm)	2.4×10^{18}	2.4×10^{18}
n_e(cm^{-3})	0.35	2×10^{-4}
$t_{acc}(Z/c)$	120	9.75×10^{-5}
u'_{ext}(erg cm^{-3})	–	3.3

is merely a parametrization of pre-acceleration throughout the jet with steady-state rate

$$Q(\gamma) = Q_0 \exp\left(-\frac{(\gamma - \gamma_{inj})^2}{2\,\sigma_\gamma^2} \right). \qquad (5)$$

The pre-accelerated particles are then subjected to stochastic acceleration in the entire simulation box. The comparison between t_{acc} and the cooling time-scale, which is energy dependent, gives the maximum energy of particles; the ratio between t_{acc} and t_{esc} decides the spectral index of the particle power-law distribution. Particle acceleration, cooling, injection, and escape reach an equilibrium, which forms the quiescent state of the system, with parameter values as listed in Table 1. The simulations need some time to reach equilibrium, and so flares are launched only when equilibrium condition have been reached.

Flares are induced by changing one or more parameters of the system in a thin zone plotted red in Fig. 2, that is assumed stationary in the host-galaxy frame and therefore propagates relativistically in the simulation frame. Such standing features can arise from external perturbations or through recollimation. We do not intend to specify the origin of the perturbation, but focus on its effect. In this paper, we specifically discuss changes in the magnetic field and in the acceleration time, t_{acc}. More details about the particle processes in our model can be found in Chen (2012). Example electron distributions in individual zones are shown in Fig. 3 and the bottom panels of Figs 5–8.

We set the angle between the line of sight and the jet axis as $\theta = 1/\Gamma$, and so the Doppler factor δ is always equal to the bulk Lorentz factor Γ. In the comoving frame of the jet, this is equivalent to observing at $90°$ to the jet axis. Except in Section 4.3, the magnetic field is assumed to be fully disordered. The conversion between flux and apparent luminosity is done with the cosmological parameters $\Omega_m = 0.28$, $\Omega_\Lambda = 0.72$, $H_0 = 70$ km s^{-1} Mpc^{-1}. A steady thermal component is added to the simulation during postprocessing, using an average thermal-emission component from radio-loud quasars (Elvis et al. 1994) scaled according to the observed *Swift*/UltraViolet and Optical Telescope (UVOT) flux of PKS 0208−512. Note that this average thermal component is directly deduced from observation, without needing to specify whether it comes from the accretion disc, X-ray corona, or anything else. All the simulated SEDs aim to match their observational counterparts from flare 2, i.e. the filled triangles in the plotted SEDs. Matching between the observational and simulation light curves is achieved through variation of the starting points, i.e. they can be shifted horizontally to match each other. In Figs 4–8, the SED and light-curve
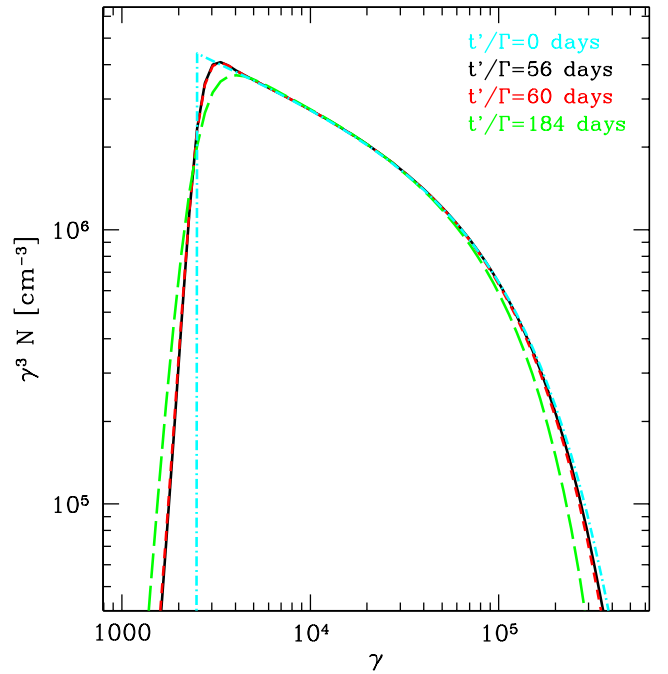

Figure 3. The electron spectrum in the bottom-centre cell (nr=1, nz=1 in Fig. 2) in the pure synchrotron self-Compton (SSC) case with change of the magnetic field as the cause of the flare. The red line corresponds to the time when the perturbation has reached the bottom zone, i.e. displays flare spectra. t'/Γ are shown for reference only. They do not correspond to any specific observer's time t because of the LTTEs.

plots have the same observational data. The pre-flare/flaring SED data are 10 d averages centred on MJD 547 25/547 35 for flare 1, and MJD 551 65/551 95 for flare 2. The historical data include (grey squares) *Swift*, *Planck*, and ground-based radio data in November of 2009 reported by Giommi et al. (2012), and (grey circles) Wide-field Infrared Survey Explorer (*WISE*) data taken in MJD 553 67–553 69 (around 2010 June 23).

4 RESULTS

4.1 Pure SSC scenario

4.1.1 Brief change of magnetic-field strength

We begin the investigation with a pure synchrotron self-Compton (SSC) scenario. In this case, five key parameters (magnetic field B, electron density n_e, volume length Z (or radius R), beaming Doppler factor δ, and Lorentz factor of the injected low-energy particle γ_{inj}) are constrained by five observables (synchrotron and IC peak frequencies ν_{sy}, ν_{ic}, synchrotron and IC apparent luminosity L_{sy}, L_{ic}, and variability time-scale t_{var}). We note that the symmetry of most light curves in blazars (similar rise and decay time, Chatterjee et al. 2012) indicates t_{var} is directly linked to LTTEs. The parameters used are summarized in Table 1.

The flare is assumed to be caused by an increase of magnetic-field energy density (by a factor of 20) immediately downstream of the stationary perturbation (Fig. 2 left, red cylinder). The thickness of the region with increased magnetic field is 1/10 of the length of the emitting blob. The same thickness is used in subsequent cases.

The resulting electron distributions are shown in Fig. 3, whereas the SEDs and the light curves are displayed in Fig. 4. Perturbations only in the magnetic field leave the electron distribution virtually
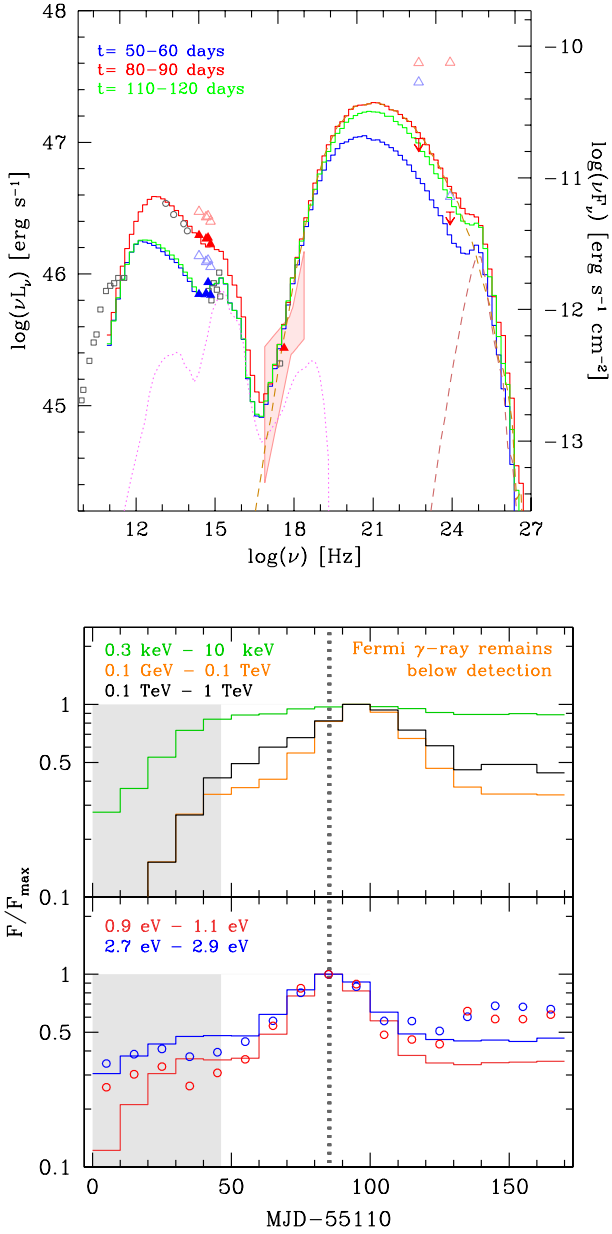
Figure 4. The SEDs (top) and light curves (bottom) in the pure SSC case with change of the magnetic field as the cause of the flare. Top: the coloured triangles are simultaneous data points from SMARTS, *Swift* and *Fermi*, with blue/red being the pre-flare/flaring states. The grey squares and circles are historical data. The open blue/red triangles are part of flare 1 identified by Chatterjee et al. (2013a), while the filled blue/red triangles are for flare 2. The *Swift* bow-tie and the *Fermi* upper limits are simultaneous with the filled red triangles. The three histograms show the simulated SEDs before, during, and after the peak of flare 2, and so they should match the filled triangles, while other data points are plotted there for reference. The dotted magenta line is the steady thermal emission component. The dashed orange/red lines refer to the first/second-order SSC emission during the peak of the flare. Bottom: in the lower panel, the open circles show the 10 d-averaged optical light curves in *B* (blue) and *J* (red) bands during flare 2. The histograms show two simulated synchrotron light curves at similar frequencies. In the upper panel, there are no observational data points. *Fermi* γ-ray flux was always below detection in 10 d bins during this time. Three simulated IC light curves are shown, with green, orange, and black solid lines representing the energy bands in X-ray, *Fermi* γ-ray, and very high energy (VHE) γ-ray. The shaded grey areas mark the phase when the simulation is still in setup phase. The vertical dotted line marks the peak of the synchrotron flare.
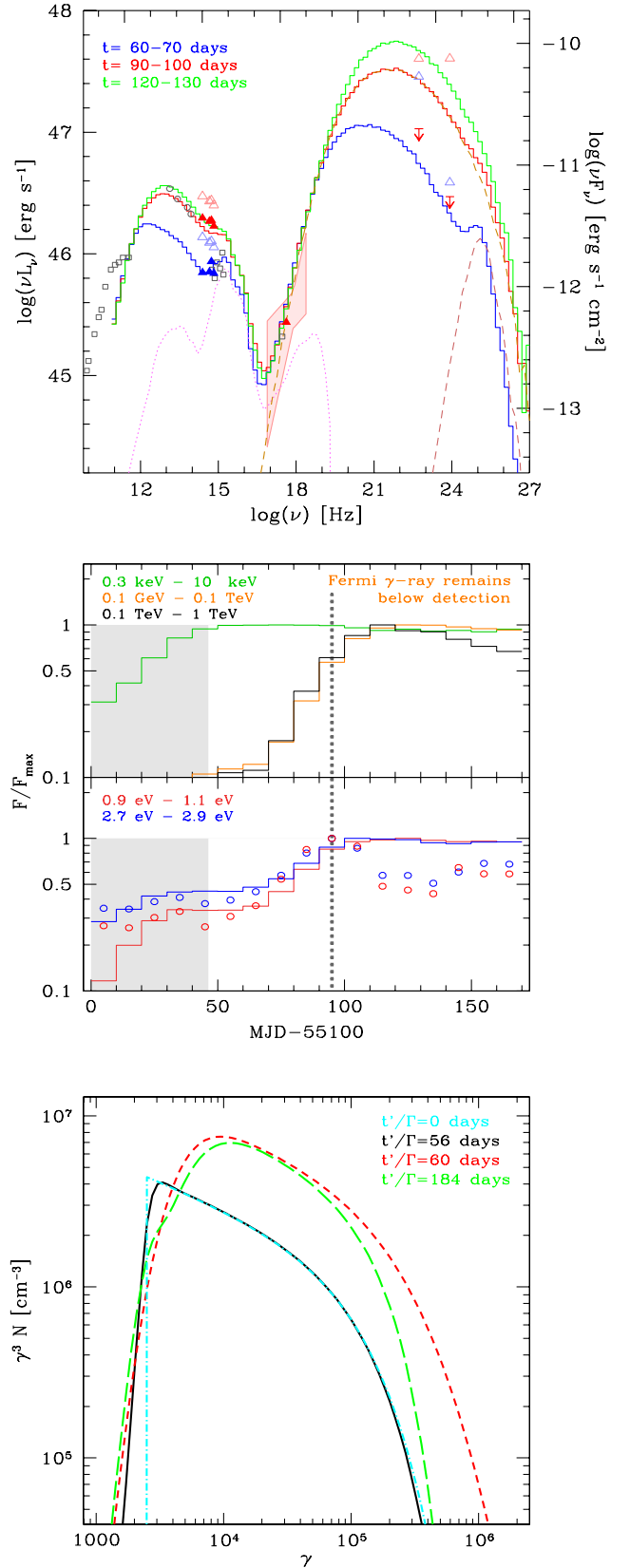
Figure 5. The SEDs (top), light curves (middle) and electron distributions (bottom) of the SSC case with change of particle acceleration efficiency as the cause of the flare. The colour schemes are similar to those in Fig. 4, except there is a 10 d shift of the observation with respect to the simulation data in order to make them more comparable.
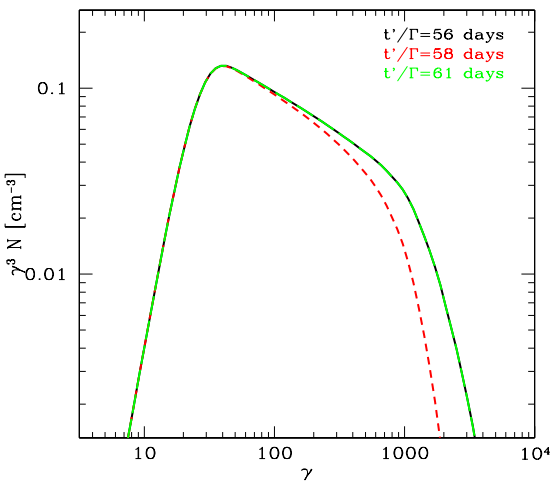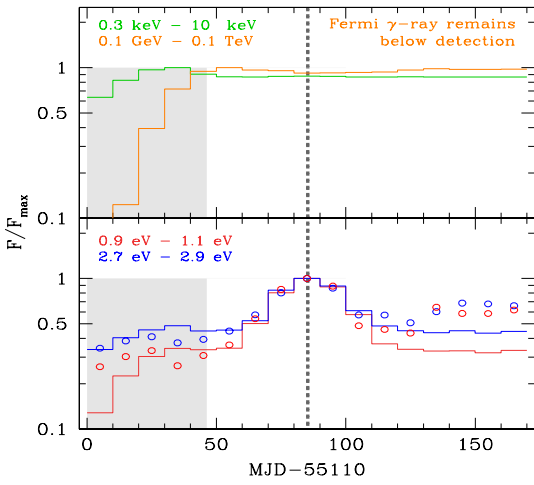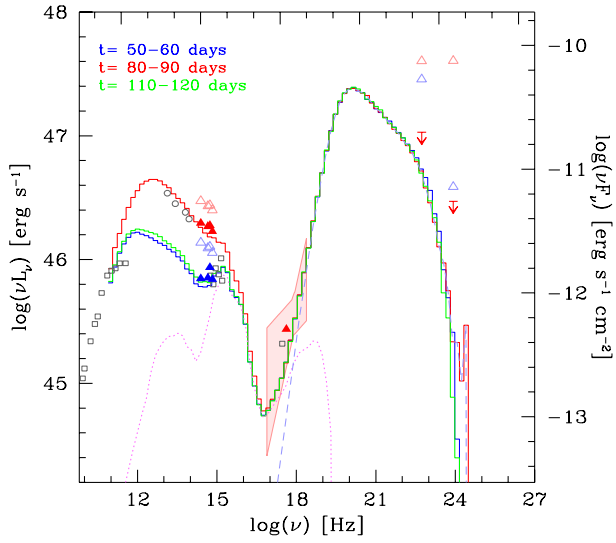
Figure 6. The SEDs (top), light curves (middle) and electron distributions (bottom) of the EC/dusty torus case with change of the magnetic field as the cause of the flare. The colour schemes are similar to those in Fig. 4, except for the EC component as blue dashed line in the SED. We also plot the SSC component, but its flux is below the flux scale shown here.
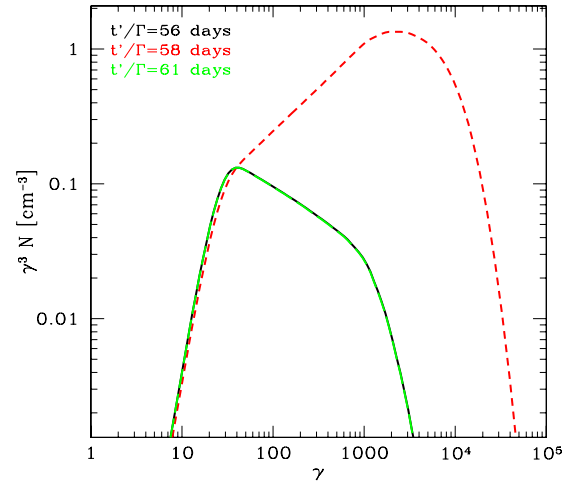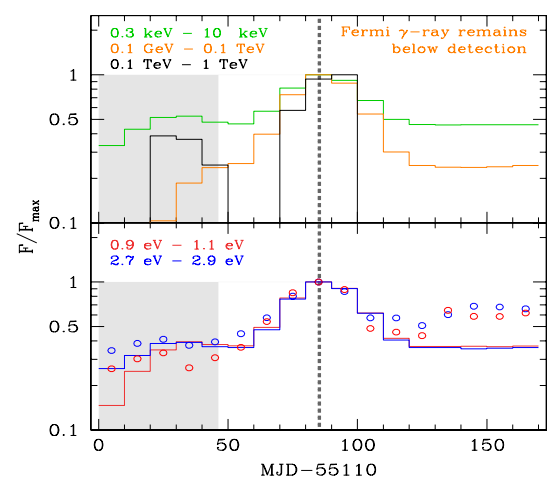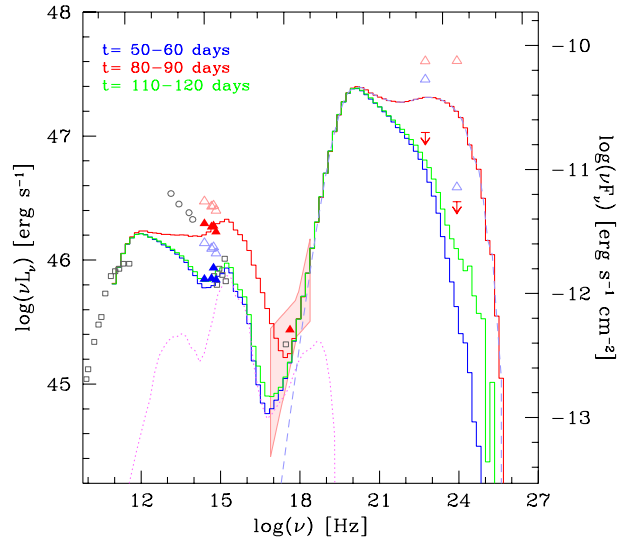
Figure 7. The SEDs (top), light curves (middle) and electron distributions (bottom) of the EC/dusty torus case with change of particle-acceleration efficiency as cause of the flare. The colour scheme is similar to that in Fig. 4, except the blue dashed line in the SED shows the EC component.
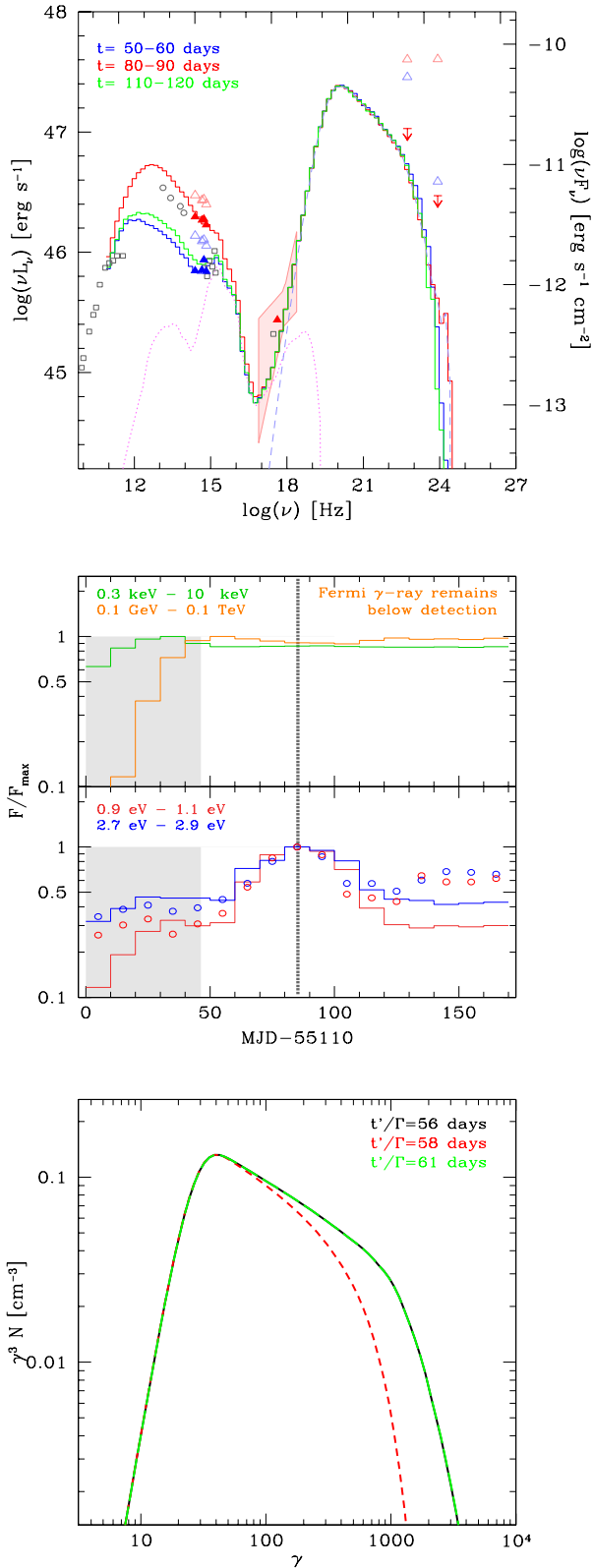
Figure 8. The SEDs (top), light curves (middle) and electron distributions (bottom) of the EC/dusty torus case with change of magnetic-field orientation as cause of the flare. The colour schemes are similar to those in Fig. 4, except the blue dashed line in the SED shows the EC component.

unchanged during the entire simulation. Variability in the radiation flux is therefore mostly caused by the modification of the emissivities and geometric effects. The blazar flares both in the optical and in γ rays, and the γ-ray flares seem to be smoother, longer lasting, and, most prominently, appear to be delayed compared to the optical flare. The delay is roughly 10 d, which is about 1/5 of the entire flare duration. Both the delay and smoothing of the γ-ray light curve are caused by the internal LTTE of the SSC emission. The inconsistency between this delay and the lack of time delays in observations such as those shown in Fig. 1 indicate that the SSC scenario with magnetic-flux change does not explain the correlated flares in FSRQs, unless the emission region is much smaller than assumed here, and the light curves are symmetric for non-geometric reasons. Neither does it explain the optical only flares, because the model predicts that the SSC flux will also increase and violate the *Fermi* upper limits in the SED.

Another interesting feature in Fig. 4 is the presence of second-order SSC emission above tens of GeV. Despite being largely suppressed by Klein–Nishina (KN) effect, the second-order SSC component is visible as an additional bump in the SED. Since the SEDs of some high-redshift blazars such as 3C 279 (MAGIC Collaboration 2008) and PKS 1424+240 (Furniss et al. 2013) appear to have an up-curving shape at VHE after the correction of extragalactic background light (EBL) absorption, it is tempting to explain those SEDs with the second-order SSC emission. However, PKS 1424+240 is classified as an intermediate-frequency peaked BL Lac or high-frequency peaked BL Lac. The higher peak energy of the synchrotron component suggests that a significant second-order SSC emission is very unlikely on account of KN suppression. Since these different types of blazars show similar up-curving SED only after EBL de-absorption, it may be more natural to explain these curves as a result of the uncertainty in the EBL models used.

4.1.2 Brief change of acceleration efficiency

Current theories of magnetic-field amplification typically involve the generation of strong turbulence (Bell 2004; Mizuno et al. 2011), which can be expected to cause strong stochastic particle acceleration. If a flare is caused by a change in the particle distribution, e.g. originating from a change in the efficiency of particle acceleration, the SSC emission would show an immediate response, long before the effect of the increase in the synchrotron seed photons becomes apparent. Then the delay between the SSC emission and synchrotron emission may be less prominent, as shown in Chen et al. (2011) for Mrk 421. We here investigate this scenario for PKS 0208−512 with time-dependent simulations, in which t_{acc} is reduced by a factor of 200 in a thin layer without any change in B. The results are shown in Fig. 5.

In the time-dependent SSC model, the model parameters are well constrained, and the resulting strength of magnetic field is only 0.4 mG in the quiescent state, making the cooling of the electrons quite slow compared to the flare time-scale. One result of this slow cooling is that any existing energized electrons, or injected new high-energy particle population (Barkov et al. 2012; Zacharias & Schlickeiser 2012), will survive for a while without being able to cool down to the quiescent state soon. This explains the electron distributions we see (Fig. 5 bottom), where the electrons are accelerated to higher energy because of the perturbation, but take a long time to cool down afterwards. The resulting light curves (except radio and X-ray) would show sharp rising time, but much longer decay time (Fig. 5 middle). However, such phenomena are not seen in observations. Therefore, the SSC with electron distribution

change scenario, including the one in which the change is caused by the increase of particle acceleration efficiency, does not explain the flares in PKS 0208−512 neither.

4.2 Dusty torus EC scenarios

Having established the difficulty to explain optical orphan flares and a lack of time delays in a pure SSC scenario, we now turn to external Compton (EC) processes as the main mechanism responsible for γ-ray emission. We chose the dusty torus as source of the soft photons. The torus is assumed to emit blackbody radiation with a temperature of about 370 K (Ghisellini & Tavecchio 2009). This external photon field is constant, if, as we do, one considers standing perturbations in the jet (for more discussion of this issue see Section 5.2). The detection of FSRQs by imaging atmospheric-Cherenkov telescopes (IACT) above 100 GeV (MAGIC Collaboration 2008; Aleksić et al. 2011; H.E.S.S. Collaboration 2013) places the γ-ray emission site outside of the broad-line region (BLR), otherwise the γ-rays would suffer catastrophic $\gamma-\gamma$ absorption with the BLR photons (Tavecchio & Ghisellini 2012). Compared to the pure SSC scenario, the EC scenario has one additional parameter, namely the energy density of the external photons. We use u'_{ext} to denote this energy density in the jet frame. This parameter is connected to the luminosity of the quasar thermal emission. However, the large uncertainty in the torus radius and covering factor means it is poorly constrained. So in the EC scenario, we fix the bulk Lorentz factor Γ (hence δ) to 40, which is the value used in the SSC scenarios and is also close to the largest value determined in very long baseline interferometry (VLBI) observation of quasar jets (Jorstad et al. 2005).

4.2.1 Brief change of magnetic-field strength

Fig. 6 shows results for the EC case with a brief change of magnetic-field strength as the cause of the flare. The magnetic-field energy density is increased by a factor of 27 in the perturbation layer.

Because stronger magnetic field imply stronger radiative cooling, the electrons change to a slightly lower energy state which, however, has minimal effects on the final radiation. The optical synchrotron emission becomes strongly variable, but the IC emissions remain quiet. This case is a fair reproduction of the observed orphan optical flares. However, to spawn orphan optical flares and the optical/γ-ray correlated flares in the same source, other processes must account for correlated flares.

4.2.2 Brief change of acceleration efficiency

Under the EC framework, we also evaluate the effect of a changing particle acceleration efficiency in a thin layer, in which t_{acc} is reduced by a factor of 2.2 without change in B. The results are shown in Fig. 7.

When the particle acceleration efficiency increases, the electron distribution does not only become harder, but also reaches a higher cut-off energy, albeit only for a short period of time (see Fig. 7 bottom), which leads to multiple observable effects.

As seen in Fig. 7, the optical and γ-ray activities are well correlated, with no noticeable delay. This demonstrates that correlated optical/γ-ray flares are possible in the EC framework. In order to keep the consistency among different cases, we use the same quiescent state parameters that are used for other cases, which matches the pre-flare SED with that of flare 2. We have also run simulations

with slightly different quiescent state parameters to match the SEDs of flare 1, which exhibits correlated optical/γ-ray flares. The results do not show any qualitative difference compared to the current case. Furthermore, the light curve of flare 1 is difficult to match accurately. It appears to be a flare complex with multiple overlapping flaring elements, rather than a single isolated flare.

Another prominent feature of the results is the spectral hardening during the flare, both in synchrotron and IC emission, which reflects the hardening of the electron spectrum. This behaviour is observed in γ-rays from *Fermi* monitored FSRQs (Abdo et al. 2010). In the narrow optical and infrared band, observations usually reveal a redder-when-brighter trend (Bonning et al. 2012), most likely due to the contamination from the quasar thermal emission, whose influence is also seen in the simulated light curves in Fig. 7. Observations in a wider far-infrared band can better resolve the spectral behaviour of the synchrotron component (see Nalewajko et al. 2012, who with *Herschel* observe a harder-when-brighter trend in PKS 1510−089).

The simulation indicates that the SED extends to higher energy during the flare, causing a significant VHE γ-ray flare on account of the higher maximum electron energy. For the same reason, the synchrotron emission also extends to higher energy, causing an ultraviolet flare and a contribution of synchrotron emission to the soft X-ray band. The available simultaneous multiwavelength data for PKS 0208−512 are insufficient to confirm the presence of these signals, but three other FSRQs have indeed been detected by Cherenkov Telescopes during flaring states (MAGIC Collaboration 2008; Aleksić et al. 2011; H.E.S.S. Collaboration 2013).

A soft-X-ray excess was recently observed from one FSRQ (PMN J2345−1555) during a major flare, accompanied by spectral hardening in GeV γ-rays (Ghisellini et al. 2013). Our simulation suggests that X-ray softening, ultraviolet/VHE γ-ray flaring, and far-infrared/γ-ray spectral hardening are typical features of correlated optical/γ-ray flares. We suggest that ultraviolet flares and a strong spectral softening in the X-ray band can be used as triggers for IACT observations in search of VHE emission from FSRQs. However, we note that even during strong flares of bright FSRQs, the predicted VHE flux is relatively low and persists only for a short period of time. This flux is likely to be even lower if EBL absorption is taken into consideration. So the observation of FSRQs with existing IACTs may remain challenging.

4.2.3 Brief change of magnetic field and acceleration

We have also explored the scenario that magnetic field strength and particle acceleration are changed simultaneously. The result reflects a mixture of the individual effects described in Sections 4.2.1 and 4.2.2. This mixture results in correlated optical/γ-ray flares, with the optical flare being stronger. The exact ratio of the flare amplitudes depends on the relative amplitude of the magnetic field/acceleration change. Both the synchrotron and IC spectra harden and extend to higher energy, but not as strongly as without magnetic-field amplification (Section 4.2.2), if the amplitude of the optical flare is still tuned to match the observation.

4.3 Brief change of magnetic-field orientation

All results described above are based on the simplification that the magnetic fields are fully disordered. These results should not change significantly, if the magnetic field is ordered and the field direction is constant in time. However, there is evidence that the polarization angles (PAs) of blazars change during flares (e.g. Larionov et al.

2008; Marscher et al. 2010), which suggests changes in the intrinsic magnetic-field direction, which can potentially lead to blazar flares as well.

To study such scenarios, we first modified the MCFP code so that it can handle anisotropic synchrotron emission from ordered magnetic fields. We assume the magnetic fields to have helical structure, which is supported by VLBI observation of radio jets (O'Sullivan & Gabuzda 2009). The angle-dependent synchrotron emissivity is calculated in a way similar to those in Jamil & Böttcher (2012). For a helical magnetic field, which has no radial component, the poloidal magnetic flux must remain constant along the jet, to ensure flux conservation. In our configuration, this means any change of the magnetic-field direction should be accompanied by a change of the magnetic-field strength in the azimuthal direction (see Fig. 2 right). An increase in the azimuthal field component may arise when the plasma passes through a compression, after which magnetic tension, reconnection, and other MHD processes relax the magnetic field to its original state. A specification of the details of this process is beyond the scope of the current paper, and we will only impose a localized enhancement in the toroidal field component and investigate its effect on the polarization of optical emission.

We calculate the time-dependent degree and angle of linear polarization of the synchrotron emission with the 3-D multizone synchrotron-polarization code 3DPol developed by Zhang, Chen & Boettcher (2014). To account for LTTEs, each axisymmetric zone is cut into 120 slices in azimuth, for each of which the 3DPol code calculates the Stokes parameters with proper transformation and retardation to observer time.

We model flares linked to a change in magnetic-field orientation in the dusty torus EC framework. The initial magnetic-field direction is at 45° to the jet axis (the poloidal and azimuthal components of the field, B_z and B_ϕ, have equal strength), while the angle is 84°.5 in a thin layer that relativistically propagates through the simulation volume. This is realized by temporarily increasing B_ϕ, while keeping B_z and the acceleration unchanged. Other parameters are identical to the other EC cases.[4]

The results are shown in Figs 8 and 9. Fig. 8 appears similar to Fig. 6 at first glance, i.e., the case with change of the B-field strength, as both of them predict flares in the optical without γ-ray counterpart. The shape of the synchrotron flares is notably different, though. A variation in the magnetic-field direction yields longer lasting high states, along with faster flux increase and decay.

The difference in apparent flare shape arises from LTTEs: the emission from the lower near part of the cylinder will arrive first, and B_ϕ fully contributes to the observed synchrotron emission, because it is locally oriented perpendicular to the line of sight. As the perturbation moves along, we observe enhanced emission from the near part of the cylinder coincidentally with that from the central parts of the cylinder (see illustration in fig. 8 of Chen et al. 2011), where the increased B_ϕ does not contribute to the observed emission, because in a helical field configuration B_ϕ is aligned with the line of sight, when the observer is located 90° from the axis. Later, when we observe enhanced synchrotron emission from the upper rear part, the enhancement in B_ϕ is again reflected in the emissivity. This explains why the flare changes rapidly at the beginning and end of the flare, while remains relatively stable around the peak.

Fig. 9 shows polarization results consistent with those presented in Zhang et al. (2014) for PKS 1510−089. The polarization degree

shows a substantial increase during the flare, except at the beginning and end of the flare, when temporary decreases are seen. This can be understood by noticing that at the beginning and end B_z dominates the polarization because it is always perpendicular to the line of sight, but around the peak of the flare B_ϕ dominates. The higher frequency band shows a smaller polarization degree because of contamination with thermal emission (the big blue bump). We also notice small dips in the polarization degree near the peak of the flare that arise from beam and line-of-sight depolarization of emission from the central region of the simulation volume.

Similar geometric effects cause the relevant PA changes shown in the right-hand panel of Fig. 9. During the first half of the flare, the emission from the near side dominates, and so the PA is close to 5°.5 (for a right-handed helix). In the second half of the flare, the PA is close to 174°.5. Before and after the flare, the emission from B_z is stronger than that from B_ϕ, and so the PA is 90°.

The lower right panel of Fig. 9 shows that, if we 'correct' the PA by forcing it to always change by less than 90°, which is a common practice in the analysis of observations (e.g. Marscher et al. 2010), a single flare can be interpreted as going through a PA rotation by 180°. If the process repeats, causing multiple flares, the total PA rotation can reach values much larger than 180°. If the magnetic helix is left handed, the rotation will progress in an opposite direction.

5 DISCUSSION

With our time-dependent inhomogeneous blazar model, we studied in both the SSC and the EC framework FSRQ flares that are caused by changes in magnetic field and particle-acceleration efficiency.

SSC models with magnetic-field change predict correlated optical/γ-ray flares, with a slight delay of the γ-ray emission. This delay is caused by the extra propagation time of synchrotron photon before the self-Compton scattering (Sokolov, Marscher & McHardy 2004). Such delays in FSRQs have not been confirmed by observations. SSC models with localized enhancement in the acceleration efficiency do not reproduce the observations either, because they generally predict flux increases without decay on the same time-scale. In particular, the orphan optical flare observed in PKS 0208−512 does not find a natural explanation in the SSC framework. All in all, the SSC scenario appears to be less favourable for FSRQs.

Using the EC framework, we reproduced both orphan optical and optical/γ-ray correlated flares with the same quiescent-state setup. In the simulation, the difference lies in the cause of the flares, i.e. whether the magnetic field or particle-acceleration efficiency is changed. From an astrophysical point of view, this difference can be tied to the allocation of free energy between magnetization and turbulence. Interestingly, this may depend on the initial orientation of the magnetic field.

MHD simulations of magnetic-field amplification (Mizuno et al. 2011, 2014) show that when the magnetic field is perpendicular to the plasma flow, compression increases the share of energy that is transferred to the large-scale magnetic field. If the magnetic field is parallel to the plasma flow, more energy is channelled into turbulent magnetic field and possibly particle acceleration. We speculate that the former case corresponds to the orphan optical flares, and the latter case corresponds to the optical/γ-ray correlated flares.

At the same time, the compression of perpendicular magnetic field should lead to a stronger optical polarization. In this interpretation, an increase in polarization degree will coincide with an increase in optical flux while its correlation with γ-ray flux will be

---

[4] This case is similar to the scenario 1 of Zhang et al. (2014), except for the choice of parameters.
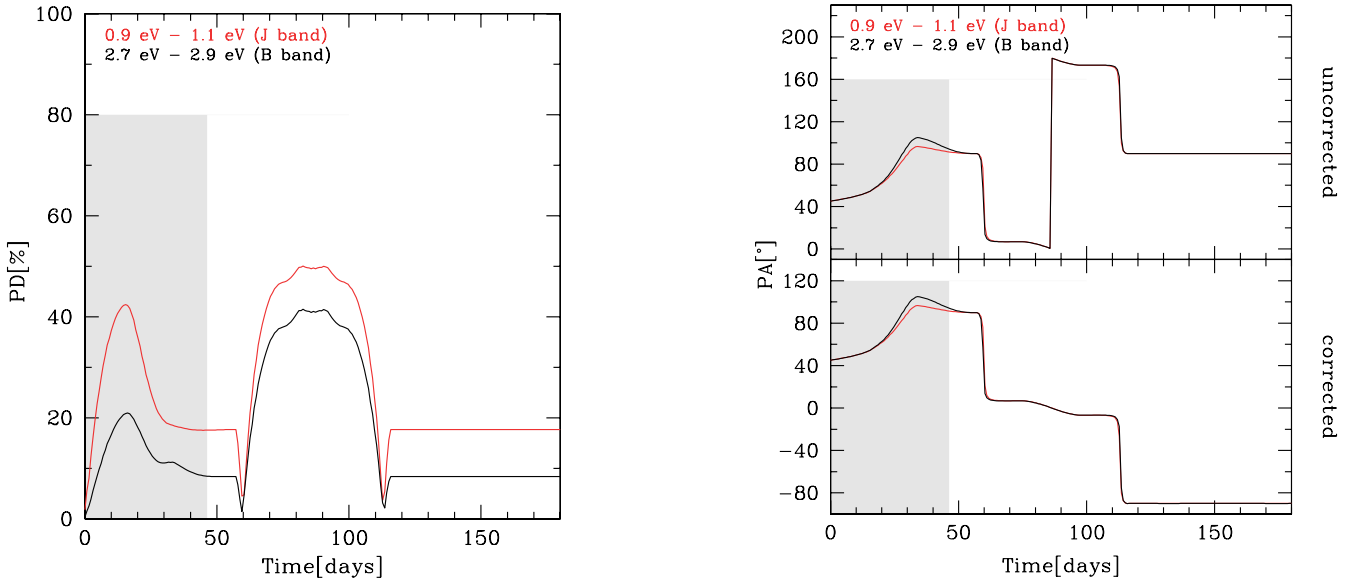
Figure 9. Synchrotron polarization degree (PD, left) and polarization angle (PA, right) for two optical bands in the EC/dusty torus scenario with change of magnetic-field orientation as cause of the flare. The shaded grey areas mark the phase when the simulation is still in setup phase. 0° of the PA is set for its electric vector to be along the jet axis. The uncorrected PAs (upper panel) are limited to [0°,180°], while the corrected PAs (lower panel) assume that any two consecutive PA values change by less than 90°.

weak. Whether such a correlation between the degree of polarization and the optical/γ-ray flux ratio exists is yet to be observationally tested.

An enhancement in particle-acceleration efficiency (possibly associated with parallel magnetic field and stronger turbulent magnetic-field amplification) in the EC framework does not only explain the optical/γ-ray correlated flares, but also produces interesting features that resemble those observed from many FSRQ flares. These include a spectral hardening of infrared and γ-ray emission, a soft-X-ray excess, and the rare detections of VHE γ-rays. All the above arise because the enhanced particle acceleration will harden the electron spectrum and extend the maximum Lorentz factor γ_{max} at the same time. Synchrotron and IC emission will simply reflect the shape of the electron spectrum. Its hardening manifests itself as spectral hardening in both the synchrotron (infrared) and the IC (γ-ray) emission, while the larger maximum Lorentz factor leads to higher cut-off energies of the two emission components. Our results also suggest that activity in the ultraviolet band and the softness of the X-ray spectrum can be important diagnostics of VHE flaring states, although VHE detection will probably remain difficult on account of the low flux even during flares and the short duration of these flares.

5.1 Ordered magnetic field and polarization

Using a simple helical magnetic field, we studied the effects of an ordered magnetic field on the multiwaveband variability and the optical polarization. The most interesting finding is that this simple scenario produces not only an orphan-optical flare, but also an increase in polarization degree and a perceived 'rotation' of PA. This 'rotation' is in parts caused by LTTEs and hence does not constitute evidence of plasma moving in a helical trajectory along the magnetic field lines of the jet (Marscher et al. 2010). If there are multiple plasma perturbations, or the plasma crosses multiple external perturbations, causing multiple flares, the measured PA rotation can be much larger than 180°. Interestingly, S5 0716+714

has been observed to show a step-like rotation of PA (Ikejiri et al. 2011), which seems to be compatible with this scenario.

Our treatment of the compression of the magnetic helix and its later relaxation are highly simplified. Detailed studies and MHD simulations are needed to elucidate the details of the scenario. We also note that a combination of ordered and disordered magnetic field must be expected and indeed appears required to produce a correlation between polarization and optical/γ-ray flux ratio, as we qualitatively discussed earlier.

5.2 External radiation field

Whereas this study only considers the dusty torus as source of external radiation, its results are qualitatively applicable to most other kinds of external photon sources. The size of the emission blob used in this study is comparable to the size of the dusty torus ($R_{ir} = 5 \times 10^{18}$ cm). If we did not consider a perturbation of the jet that is stationary in the host-galaxy frame, this perturbation would travel a significant distance during a single flare, and consequently would experience a considerable variation of the external photon density. We can expect that perturbations travelling down the jet can cause a decrease in the γ-ray emission, on account of the changes in the external radiation field (Dermer, Schlickeiser & Mastichiadis 1992; Dermer & Schlickeiser 2002), while the optical emission remains steady.

5.3 Particle escape

The rate of particle escape required for PKS 0208−512 in the EC scenario is very high. The very efficient radiative cooling mandates that the acceleration time be $t_{acc} \sim 10^{-4}R/c$, otherwise particles cannot be accelerated to $\gamma \sim 1000$. The spectral index of the particle distribution on the other hand requires the ratio t_{acc}/t_{esc} to be about 6.5. Therefore, t_{esc} needs to be as short as $1.5 \times 10^{-5}R/c$. This particle escape is too fast to be explained by particle streaming out of the emission region.

One possible explanation is that the particles are accelerated in much smaller turbulent cells (see Marscher 2013, for discussion of the idea of turbulent cells). So the 'escape' used in our model does not represent escape from the emission region, but rather escape from the accelerators. For example, if the size of the turbulent cells is $R_{cell} = 10^{-5}R/c$, then $t_{esc} = 1.5R_{cell}/c$. An ensemble of such small acceleration zones might exist in the jet, whose large-scale distribution may be planar as assumed in this work or follow a different geometry. In this interpretation, the escaped particles are no longer being accelerated, but still contained in the jet, and would thus still contribute to both synchrotron and IC emission. Our treatment of particle and radiation spectra does not properly account for this possibility. Instead, we ignore the escaped particles and effectively model the emission behaviour of the particles in the accelerators.

In fact, particle escape from jet emission zones is a widespread but questionable concept, because at least IC scattering of ambient radiation is unavoidable and the emission from the escaped particles may well dominate over those residing in the accelerator region. In this work, we do not directly model the escaped particle population, because simplifications such as the energy independence of the acceleration time-scale or the constant Lorentz factor of the jets (i.e., the absence of internal shocks in the model) may be as influential in driving the parameters.

Here, our emphasis was on exploring the impact of LTTEs. A forthcoming paper shall investigate small-scale acceleration zones embedded in a larger jet. For that purpose, we shall add diffusive transport to the code to self-consistently model the three-dimensional expansion of a cloud of flare electrons that are produced in a small volume. As the geometry of the emission region is a critical parameter in modelling blazar flares (Sokolov et al. 2004; Sokolov & Marscher 2005), we may find that a different particle escape rate is needed to maintain the same characteristics of the SED. As this time, all parameters should be taken *cum grano salis*.

6 CONCLUSIONS

Using our 2-D Monte Carlo/Fokker–Planck code, we have modelled FSRQ flares with several scenarios related to magnetic-field amplifications. Changes in the magnetic-field strength, its orientation, and the particle-acceleration efficiency have been explored as causes of flares, with either the SSC or the EC mechanism producing the γ-ray emission.

We conclude this paper with the following findings regarding FSRQs.

(i) SSC scenarios are disfavoured because they do not naturally produce orphan-optical flares, and even for optical/γ-ray correlated flares, the model either predicts a delay of γ-ray flare, or the flux would not subside after the flare.

(ii) The difference between orphan optical and optical/γ-ray correlated flares can be understood as being caused by different initial orientation of the magnetic field in the plasma and subsequent effects on magnetic-field amplification.

(iii) Changes in the particle-acceleration efficiency in an EC model can explain several features observed during flares, including:

(a) spectral hardening of infrared and γ-rays;
(b) X-ray soft-excess;
(c) rare detections of VHE γ-rays.

(iv) A correlation may exist between optical polarization degree and optical/γ-ray flux ratio.

(v) The polarization degree change and PA rotation of $\geq 180°$ can be explained by compression and subsequent relaxation of helical magnetic fields in combination with LTTEs.

REFERENCES

Abdo A. A. et al., 2010, ApJ, 710, 1271
Aleksić J. et al., 2011, ApJ, 730, L8
Barkov M. V., Aharonian F. A., Bogovalov S. V., Kelner S. R., Khangulyan D., 2012, ApJ, 749, 119
Bell A. R., 2004, MNRAS, 353, 550
Bonning E. et al., 2012, ApJ, 756, 13
Bregman J. N., Glassgold A. E., Huggins P. J., Lebofsky M. J., Rieke G. H., Aller M. F., Aller H. D., Hodge P. E., 1981, Nature, 293, 714
Chatterjee R. et al., 2012, ApJ, 749, 191
Chatterjee R. et al., 2013a, ApJ, 763, L11
Chatterjee R., Nalewajko K., Myers A. D., 2013b, ApJ, 771, L25
Chen X., 2012, PhD thesis, Rice University
Chen X., Fossati G., Liang E. P., Böttcher M., 2011, MNRAS, 416, 2368
Chen X., Fossati G., Böttcher M., Liang E., 2012, MNRAS, 424, 789
Dermer C. D., Schlickeiser R., 2002, ApJ, 575, 667
Dermer C. D., Schlickeiser R., Mastichiadis A., 1992, A&A, 256, L27
Elvis M. et al., 1994, ApJS, 95, 1
Evans P. A. et al., 2009, MNRAS, 397, 1177
Fraschetti F., 2013, ApJ, 770, 84
Furniss A. et al., 2013, ApJ, 768, L31
Ghisellini G., Tavecchio F., 2009, MNRAS, 397, 985
Ghisellini G., Tavecchio F., Foschini L., Ghirlanda G., 2011, MNRAS, 414, 2674
Ghisellini G., Tavecchio F., Foschini L., Bonnoli G., Tagliaferri G., 2013, MNRAS, 432, L66
Giommi P. et al., 2012, A&A, 541, A160
Guo F., Li S., Li H., Giacalone J., Jokipii J. R., Li D., 2012, ApJ, 747, 98
H. E. S. S. Collaboration, 2013, A&A, 554, A107
Healey S. E. et al., 2008, ApJS, 175, 97
Ikejiri Y. et al., 2011, PASJ, 63, 639
Impey C. D., Neugebauer G., 1988, AJ, 95, 307
Jamil O., Böttcher M., 2012, ApJ, 759, 45
Jorstad S. G. et al., 2005, AJ, 130, 1418
Katarzyński K., Ghisellini G., Mastichiadis A., Tavecchio F., Maraschi L., 2006, A&A, 453, 47
Krawczynski H. et al., 2004, ApJ, 601, 151
Larionov V. M. et al., 2008, A&A, 492, 389
MAGIC Collaboration, 2008, Science, 320, 1752
Marscher A. P., 1998, in Zensus J. A., Taylor G. B., Wrobel J. M., eds, ASP Conf. Ser. Vol. 144, IAU Colloq. 164: Radio Emission from Galactic and Extragalactic Compact Sources. Astron. Soc. Pac., San Francisco, p. 25
Marscher A. P., 2013, preprint (arXiv:e-prints)
Marscher A. P. et al., 2010, ApJ, 710, L126

Mizuno Y., Pohl M., Niemiec J., Zhang B., Nishikawa K.-I., Hardee P. E., 2011, ApJ, 726, 62

Mizuno Y., Pohl M., Niemiec J., Zhang B., Nishikawa K.-I., Hardee P. E., 2014, MNRAS, 439, 3490

Nalewajko K., Sikora M., Madejski G. M., Exter K., Szostek A., Szczerba R., Kidger M. R., Lorente R., 2012, ApJ, 760, 69

O'Sullivan S. P., Gabuzda D. C., 2009, MNRAS, 393, 429

Parizot E., Marcowith A., Ballet J., Gallant Y. A., 2006, A&A, 453, 387

Pohl M., Schlickeiser R., 2000, A&A, 354, 395

Sambruna R. M., Maraschi L., Urry C. M., 1996, ApJ, 463, 444

Schlickeiser R., 1984, A&A, 136, 227

Sokolov A., Marscher A. P., 2005, ApJ, 629, 52

Sokolov A., Marscher A. P., McHardy I. M., 2004, ApJ, 613, 725

Stroh M. C., Falcone A. D., 2013, ApJS, 207, 28

Tavecchio F., Ghisellini G., 2012, preprint (arXiv:e-prints)

Urry C. M., Mushotzky R. F., 1982, ApJ, 253, 38

Zacharias M., Schlickeiser R., 2012, ApJ, 761, 110

Zhang H., Chen X., Boettcher M., 2014, ApJ, preprint (arXiv:1401.7138)

This paper has been typeset from a TEX/LATEX file prepared by the author.